Inorganic Chemistry
Cite This: Inorg. Chem. 2019, 58, 13464−13470
Article
pubs.acs.org/IC

Lead-Free Hybrid Metal Halides with a Green-Emissive [$MnBr_4$] Unit as a Selective Turn-On Fluorescent Sensor for Acetone

Mingze Li,[#,†] Jun Zhou,[#,†] Maxim S. Molokeev,[‡,§,⊥] Xingxing Jiang,[▽] Zheshuai Lin,[▽] Jing Zhao,[†] and Zhiguo Xia*[,†,¶]

[†]The Beijing Municipal Key Laboratory of New Energy Materials and Technologies, School of Materials Sciences and Engineering, University of Science and Technology Beijing, Beijing 100083, China

[‡]Laboratory of Crystal Physics, Kirensky Institute of Physics, Federal Research Center KSC SB RAS, Krasnoyarsk 660036, Russia

[§]Siberian Federal University, Krasnoyarsk 660041, Russia

[⊥]Department of Physics, Far Eastern State Transport University, Khabarovsk, 680021, Russia

[▽]Technical Institute of Physics and Chemistry, Chinese Academy of Sciences, Beijing 100190, China

[¶]State Key Laboratory of Luminescent Materials and Devices and Institute of Optical Communication Materials, South China University of Technology, Guangzhou 510641, China

Supporting Information

ABSTRACT: Organic−inorganic hybrid metal halides with zero-dimensional (0D) structure has emerged as a new class of light-emitting materials. Herein, a new lead-free compound $(C_9NH_{20})_2MnBr_4$ has been discovered and a temperature-dependent phase transition has been identified for two phases (space group $P2_1/c$ and $C2/c$) in which individual $[MnBr_4]^{2-}$ anions connect with organic cations, $(C_9NH_{20}^+)$ (1-buty-1-methylpyrrolidinium$^+$), forming periodic structure with 0D blocks. A green emission band, peaking at 528 nm with a high photoluminescence quantum efficiency (PLQE) of 81.08%, has been observed at room temperature, which is originated from the $^4T_1(G)$ to $^6A_1$ transition of tetrahedrally coordinated Mn^{2+} ions, as also elaborated by density functional theory calculation. Accordingly, a fast, switchable, and highly selective fluorescent sensor platform for different organic solvents based on the luminescence of $(C_9NH_{20})_2MnBr_4$ has been developed. We believe that the hybrid metal halides with high PLQE and the exploration of these as a fluorescence sensor will expand the applications scope of bulk 0D materials for future development.

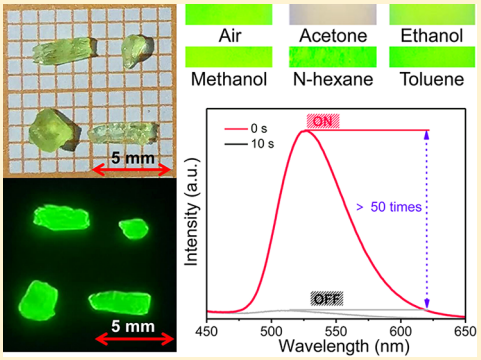

INTRODUCTION

Establishing a framework with functional units and the rational design of new organic−inorganic hybrid metal halides enable the expansion of the database of emerging materials,[1−3] especially since they will contribute to different optoelectronic applications, including photodetectors,[4,5] solar cells,[6−8] light-emitting diodes (LEDs),[9,10] and so on. Among these, zero-dimensional (0D) metal halides with broad-band emission and high exciton binding energies become star materials with unprecedented optoelectronic properties,[11−13] in which the metal−halide inorganic anionic polyhedrons are totally isolated from each other by large organic cations. To date, many organic−inorganic metal halide hybrids with 0D structure have been reported as efficient emitters, such as $(C_9NH_{20})_2SnBr_4$,[14] $(C_9NH_{20})_7(PbCl_4)Pb_3Cl_{11}\cdot CH_3CN$,[15] $(C_5H_7N_2)_2MBr_4$ (M = Hg and Zn)[16] and $(C_8NH_{12})_4Bi_{0.57}Sb_{0.43}Br_7\cdot H_2O$,[17] among others. Recently, our group also reported a broad-band green-emitting compound $(C_9NH_{20})_6Pb_3Br_{12}$, and the emission is attributed to the intrinsic vacancies, not the normally self-trapped excitons (STEs).[18] Currently reported 0D materials are mostly based on Pb or Sn; however, the toxicity of Pb and the instability of Sn further limit the commercial application of 0D materials. Therefore, exploring new, stable, nontoxic, high-efficiency luminescent 0D materials is a key challenge to be addressed.

Luminescent probes and sensors with superfast responsibility and ultrahigh sensitivity under different conditions (temperature, gases, pH, etc.) are essential in versatile application fields,[19] among which fluorescent gas sensing for the detection of toxic and volatile gases has received extensive attention.[20] A number of light-emitting materials including conjugated polymers, quantum dots, and organic dyes have been recently investigated as the fluorescence sensor.[21] Due to their superior optical properties and structural adjustability, luminescent metal halides are good candidates for fluorescence sensors. However, to the best of our knowledge, there are few reports on this issue.[22] Therefore, applying 0D materials with

Received: August 6, 2019
Published: September 10, 2019

DOI: 10.1021/acs.inorgchem.9b02374
Inorg. Chem. 2019, 58, 13464−13470

excellent gas sensing properties to the sensing fields is a promising route.

Here, a new lead-free metal halide $(C_9NH_{20})_2MnBr_4$ is designed and discovered from the nominal composition of previously reported $(C_9NH_{20})_6Pb_3Br_{12}$ through alloying Mn^{2+} into the lead halide inorganic framework with compelete Pb/Mn replacement.[18] However, newly discovered $(C_9NH_{20})_2MnBr_4$ possesses a crystal structure totally different from that of the Pb analog, and the individual $[MnBr_4]^{2-}$ tetrahedrons are completely isolated and surrounded by large organic cation $C_9NH_{20}^+$ (1-buty-1-methylpyrrolidinium$^+$) to form the 0D structure. Moreover, an interesting phase transition near room temperature (RT) has be found in this compound. Such a metal halide at RT exhibits a green emission band peaking at 528 nm with a high photoluminescence quantum efficiency (PLQE) of 81.08%, attributed to the transition of tetrahedrally coordinated Mn^{2+} in $[MnBr_4]^{2-}$ anions instead of excited-state structure reorganization.[23] Interestingly, the bright green emission is rapidly quenched within 10 s after injecting acetone vapor, and no obvious changes were observed with other organic vapors. High efficiency luminescence, quick response, and good selectivity shows the outstanding gas sensitivity of $(C_9NH_{20})_2MnBr_4$. This work will expand the 0D hybrid materials family and provides a possible direction of application for luminescent metal halides.

EXPERIMENTAL SECTION

Materials and Preparation. All chemicals were commercially purchased and used without further purification. Manganese(II) bromide hydrate ($MnBr_2$) (99.9%) and 1-buty-1-methylpyrrolidinium bromide ($C_9NH_{20}Br$) (99%) were purchased from Aladdin Co., Ltd. (Shanghai, China). Hydrobromic acid (48% H_2O solution) was purchased from Energy Chemical (Shanghai, China). As a typical process, 0.002 mol of $C_9NH_{20}Br$ and 0.001 mol of $MnBr_2$ were dissolved in 1 mL of HBr under heating and continuous stirring at 373 K. Then, the green crystals of $(C_9NH_{20})_2MnBr_4$ were obtained by slowly cooling the saturated solution to room temperature.

Turn-On Fluorescent Sensor Treatment. Powder samples of ground $(C_9NH_{20})_2MnBr_4$ crystals were used for sensing experiments. For each experiment, 100 mg of $(C_9NH_{20})_2MnBr_4$ was put in a small bottle. Different organic vapors are produced by using a water bath at 323 K. The vapors were injected by a microsyringe.

Characterization. A single crystal with dimensions of 0.1 × 0.1 × 0.1 mm^3 was used to collect the data at 150 K using the XtaLAB AFC12 X-ray four-circle single-crystal diffractometer (Rigaku) equipped with a CCD-detector, graphite monochromator, and Cu Kα radiation source. The orientation matrix and cell parameters were defined and refined for the set of 10 231 reflections. The unit cell corresponds to monoclinic symmetry. Space group $P2_1/c$ was determined from the statistical analysis of the intensities of all the reflections. The absorption correction using spherical harmonics was applied by ABSPAK program. The structure was solved by the direct methods using package SHELXS and refined in the anisotropic approach for non-hydrogen atoms using SHELXL program.[24] All the hydrogen atoms of the (C_9NH_{20}) ligand were positioned geometrically as riding on their parent atoms with d(C−H) = 0.93 Å for the C−H bonds and U_{iso}(H) = 1.2U_{eq}(C). The structural tests for the presence of missing symmetry elements and possible voids were produced using the PLATON program.[25] The DIAMOND program[26] is used for the crystal structure plotting. The temperature-dependent powder X-ray diffraction (PXRD) data were collected on X'Pert MRD diffractometer, and the sample was cooled in a liquid nitrogen cryostat. The structural parameters defined by single-crystal analysis were used as a basic in powder pattern Rietveld refinement. The refinement was produced using TOPAS 4.2 software.[27] The morphology and particle size of the powder sample was characterized by scanning electron microscope (SEM, JEOL JSM-6510). Elemental analysis (EA) of the samples (C, H, and N) was performed in a vario MACRO cube (Elementar Analysensysteme Gmbh, Germany). Differential scanning calorimetry (DSC) was measured by a DSC ins Q2000 V24.11 Build 124 at 20 °C min^{-1} in an argon flow from 280 to 310 K. The RT excitation (PLE), RT emission spectra (PL), the RT decay curves, and photoluminescence quantum efficiency (PLQE) were obtained using a FLSP9200 fluorescence spectrophotometer (Edinburgh Instruments Ltd., U.K.). Thermogravimetric analysis (TGA) was performed on a Setaram Labsys Evo at 10 °C min^{-1} in an argon flow from room temperature to 800 °C. The diffuse reflection spectra were measured on a UV−vis−NIR spectrophotometer (SHIMADZU UV-3600) supplied with an integrating sphere. To test the photostability, a 100 W 20 V mercury short arc lamp was used as a continuous irradiation light source. The intensity of the irradiation was calibrated to 300 mW/cm^2. The photoluminescence was measured at periodic intervals on a HORIBA iHR320 spectrofluorimeter, equipped with a HORIBA Synapse CCD detection system.

Computational Methodology. The first-principles electronic structure calculation was carried out by CASTEP, a package based on plane-wave pseudopotential density functional theory (DFT).[28] The exchange-correlation terms in the Hamiltonian were described by the function developed by Ceperley, Alder, Perdew, and Zunger (CA-PZ)[29] in the form of local density approximation (LDA).[30] The effective interaction between the atomic cores and valence electrons were treated by ultrasoft pseudopotentials, which allow us to employ a relatively small plane-wave basis set without compromising the computational accuracy. The kinetic energy cuttoff 400 eV and intensive Monkhorst−Pack k-point mesh spanning less than 0.04/Å^3 were chosen. To account for the effect of the delocalized d-orbitals in manganese atoms, the LDA+U method[24] was adopted in the calculation with the Ud set to 4.0 eV.

RESULTS AND DISCUSSION

The optical photographs of the well-developed $(C_9NH_{20})_2MnBr_4$ crystals (~5 mm) in daylight and upon 365 nm UV light excitation are shown in Figure 1a,b,

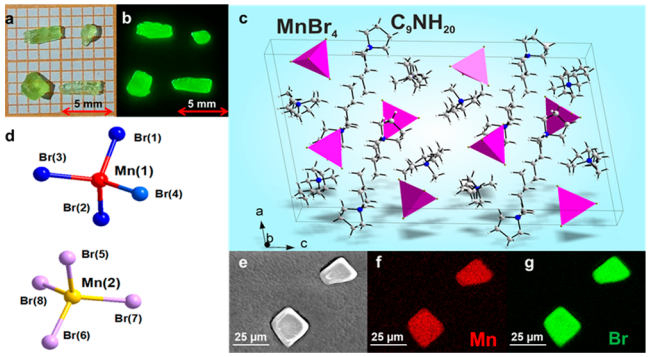

Figure 1. Optical photographs of as-grown $(C_9NH_{20})_2MnBr_4$ crystals in the daylight (a) and upon 365 nm UV excitation (b). (c) Unit cell structure model of $(C_9NH_{20})_2MnBr_4$. (d) Ball-and-stick model of $[MnBr_4]^{2-}$ tetrahedra. (e) SEM image of $(C_9NH_{20})_2MnBr_4$ microcrystals. Element mapping images of Mn (f) and Br (g).

respectively. The excellent transmittance in Figure 1a verifies the high crystal quality, and a bright green emission (Figure 1b) is observed by the naked eye upon the excitation of 365 nm UV light. The crystal structure of $(C_9NH_{20})_2MnBr_4$ was determined using single-crystal X-ray diffraction (SCXRD) at 150 K. The detailed structural parameters extracted from the refinements of $(C_9NH_{20})_2MnBr_4$ including fractional atomic coordinates, isotropic displacement parameters and main bond lengths are shown in Tables S1 and S2. CCDC 1945705

DOI: 10.1021/acs.inorgchem.9b02374
Inorg. Chem. 2019, 58, 13464−13470

contains the supplementary crystallographic data for this paper. One Alert B was generated by CheckCif program with notation "Low Bond Precision on C−C Bonds −0.015 Å". The structure is complex, and there are 451 refined parameters in total. Therefore, high intensities of reflections are needed. However, the experiment was conducted at 150 K using liquid nitrogen which means limited experiment time and that the crystals weakly reflect X-rays. Thus, relatively low bond precision was obtained. This compound demonstrates a 0D structure with the individual $MnBr_4^{2-}$ anions surrounded by large $C_9NH_{20}^{+}$ cations at the molecular level (Figure 1c). The local structures of the isolated $MnBr_4^{2-}$ anion units are shown in Figure 1d, and two nearly equivalent Mn^{2+} sites can be identified. Moreover, similar structures with different organic ligand have also been reported in other studies.[22,31,32] Figure 1e shows the SEM photograph of the powder sample (~25 μm), and the elemental mapping images in Figure 1f,g verified the homogeneous distribution of Mn and Br. In addition, EA results offered in Table S3 confirmed the composition of organic cations, which is basically consistent with the theoretical chemical constituents of $(C_9NH_{20})_2MnBr_4$.

An interesting result is that the PXRD patterns measured at RT are inconsistent with those measured from single-crystal determination at 150 K. Therefore, we reasonably believe that the material has a temperature-dependent structural phase transition, which thus produces the formation of low-temperature phase (LTP) and high-temperature phase (HTP). Figure 2a gives the temperature-dependent PXRD patterns of $(C_9NH_{20})_2MnBr_4$ from 123 to 323 K, demonstrating the phase transition process and the corresponding temperature. Figure 2b gives the amplified diffractions patterns from 17 to 27°, from which we can clearly see two kinds of diffraction patterns with minor differences below 283 K and above 303 K. The Rietveld refinement results of the selected patterns at 123 and 303 K (Figure S1) show that they are both pure phases but belong to two different space groups, $P2_1/c$ and $C2/c$, respectively. Furthermore, the PXRD patterns change reversibly to HTP and LTP during heating/cooling cycles, indicating the reversibility of phase transition (Figure S2).Table 1 gives the main crystal structure parameters of two phases. Furthermore, differential scanning calorimetry (DSC) measurement provides detailed phase transition information on $(C_9NH_{20})_2MnBr_4$ (Figure 2c). In the process of first heating and then cooling, the heat flow which depends on temperature shows an abnormal peak at 301.4 K during heating and at 298.1 K during cooling, respectively. The phenomenon of hysteresis corresponds to the first-order phase transition. In addition, the thermogravimetric-differential thermogravimetric (TGA-DTG) data of $(C_9NH_{20})_2MnBr_4$ measured from 289 to 1073 K (Figure S3) shows no change in weight during the temperature range of the possible phase transition process. All the above results confirm that there is a structural phase transition at about 301.4 K. Two phases with different space groups but the same monoclinic system were produced, and the observed phase transition may be associated with the degree order of organic cation $C_9NH_{20}^{+}$; however, the same 0D blocks with individual $[MnBr_4]^{2-}$ tetrahedrons are kept for both phases.

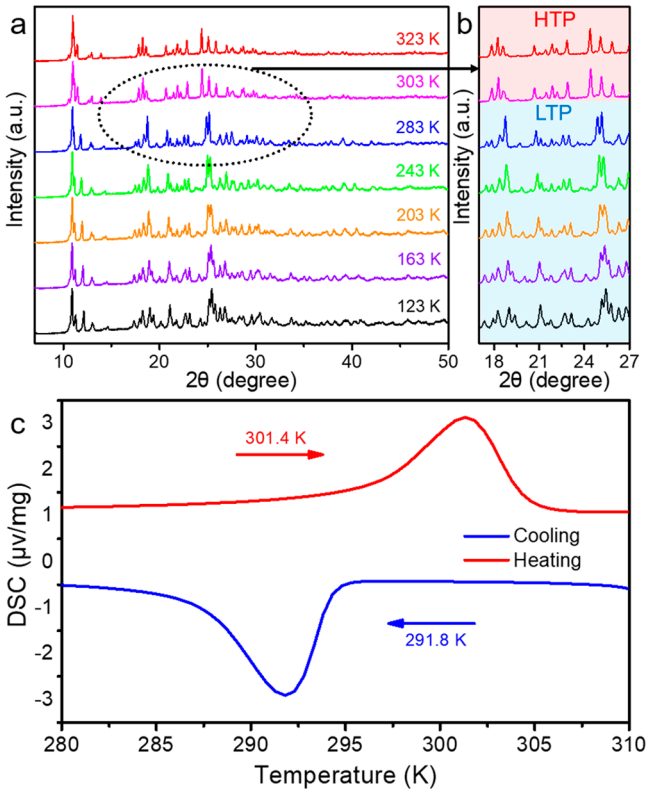

Figure 2. (a) PXRD patterns of $(C_9NH_{20})_2MnBr_4$ from 123 to 323 K. The dotted oval represents the minor change of the diffraction peaks between 283 and 303 K. (b) Amplified temperature dependent diffraction patterns from 17 to 27°. (c) DSC curves during heating and cooling of $(C_9NH_{20})_2MnBr_4$ measured between 280 and 310 K.

Table 1. Comparison of the Crystal Structure Parameters of $(C_9NH_{20})_2MnBr_4$ Measured at Different Temperatures

temperature	150 K	303 K
space group	$P2_1/c$	$C2/c$
a (Å)	17.0945(4)	16.2804(10)
b (Å)	10.2445(4)	10.1933(7)
c (Å)	30.165(1)	17.3112(11)
β (deg)	100.310(3)	110.138(3)
V (Å^3)	5197.4(3)	2697.2(3)

Figure 3a illustrates the photoluminescence emission (PL) and excitation (PLE) spectra of $(C_9NH_{20})_2MnBr_4$ at RT. The PLE spectrum of $(C_9NH_{20})_2MnBr_4$ consists of five bands around 277, 291, 362, 373, and 469 nm, corresponding to the electronic transition from the $^6A_1$ (^6S) ground state of Mn^{2+} to $^4E(D)$ (277 nm), $^4T_2(D)$ (291 nm), [$^4A_1(G)$, $^4E(G)$] (362 nm), $^4T_2(G)$ (373 nm), and $^4T_1(G)$ levels (469 nm), respectively. The PL spectra at diverse excitation wavelengths (277, 291, 362, 373, and 450 nm) are also presented in Figure 3a. The emission peak is located at 528 nm with a full width at half-maximum (fwhm) of 64 nm, which is attributed to the $^4T_1(G)$ to $^6A_1$ radiative transition of tetrahedrally coordinated Mn^{2+} ions in $[MnBr_4]^{2-}$ unit, and the asymmetric spectral profile is related with the two nearly equivalent Mn sites, as shown in Figure 1d.[33−36] Furthermore, the emission peak does not shift depending on different excitation wavelengths, confirming the intrinsic emission properties of the $(C_9NH_{20})_2MnBr_4$ crystals originating from Mn^{2+} emission centers. Considering the existence of the temperature-dependent structural phase transitions, we also compared the PL spectra at low and high temperatures (Figure 3b), which correspond to LTP and HTP, respectively. Upon excitation at

DOI: 10.1021/acs.inorgchem.9b02374
Inorg. Chem. 2019, 58, 13464−13470

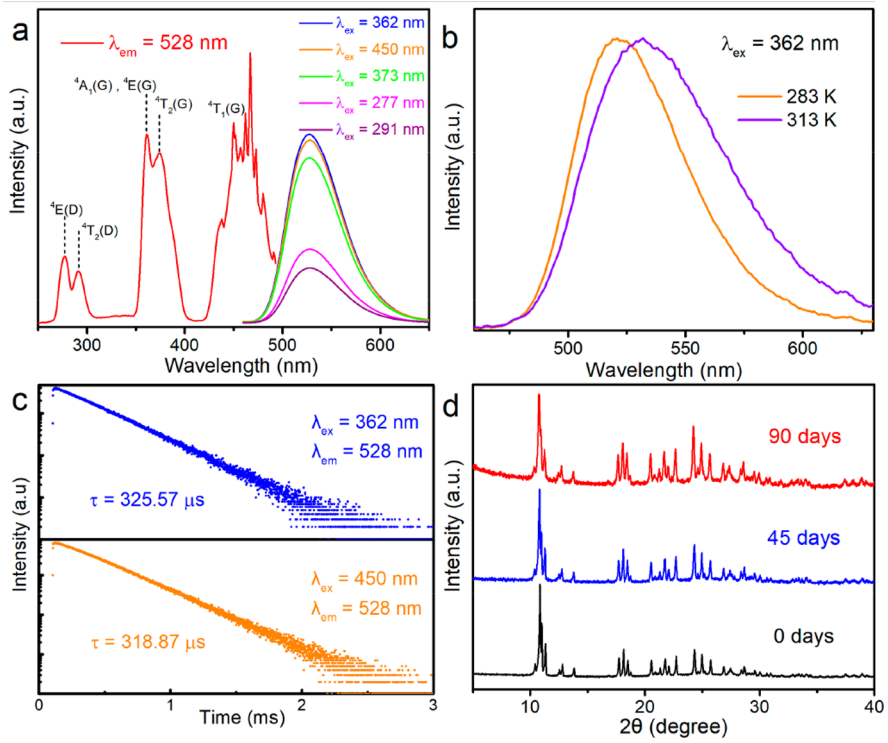

Figure 3. (a) PLE and PL spectra of $(C_9NH_{20})_2MnBr_4$ at RT. (b) PL spectra of $(C_9NH_{20})_2MnBr_4$ measured at 283 and 313 K upon the excitation of 362 nm. (c) Photoluminescence decay curves of $(C_9NH_{20})_2MnBr_4$ crystals monitored at 528 nm excited at 362 and 450 nm at RT. (d) PXRD patterns of $(C_9NH_{20})_2MnBr_4$ after 0, 45, and 90 days of exposure to light and moisture conditions.

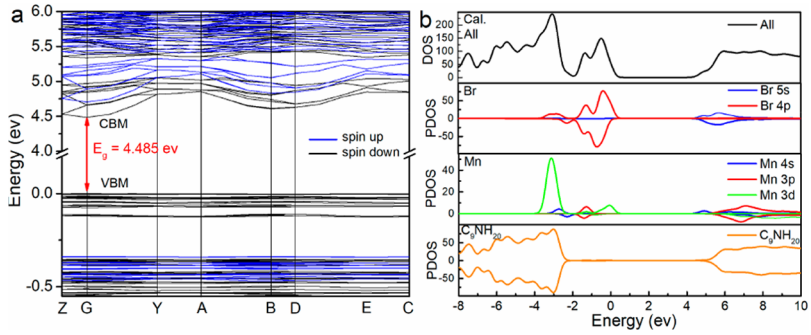

Figure 4. (a) Electronic band structure of $(C_9NH_{20})_2MnBr_4$ calculated with the DFT-PBE method. (b) Total and orbital-projected PDOS of $(C_9NH_{20})_2MnBr_4$ using DFT-PBE method.

362 nm, the PL spectral profiles are almost the same except for a little shift of emission peak, showing that phase transition has no major effect on the photoluminescence emission.

To further study the photoluminescence properties of $(C_9NH_{20})_2MnBr_4$, the PLQE at 298 K is calculated to be about 81.08%, and the CIE chromaticity coordinate for this green emission is determined to be (0.279, 0.645) (Figure S4). The RT decay curves monitoring the emission peak at 528 nm measured upon the excitation of 362 and 450 nm are depicted in Figure 3c. All the decay curves are well-fitted with a single-exponential decay function, and the effective decay times are calculated to be 325.57 and 318.87 μs, respectively. Such a long lifetime further confirms that the green emission originates from $^4T_1(G)$ to $^6A_1$ transition of tetrahedrally coordinated Mn^{2+}, which is significantly different from the reorganization of excited-state structure of other 0D materials. Furthermore, considering that the stability of hybrid metal halides is an important criterion to access their potential for practical applications, the stabilities on exposure to air, chemicals, and light under a high-power mercury lamp (300 mw cm^{-2}) with continuous irradiation illumination were measured and evaluated, respectively. Figure 3d shows the PXRD of $(C_9NH_{20})_2MnBr_4$ after exposure to an ambient atmosphere under both air and moisture conditions for different days, and the phase structures remain nearly invariable. After 90 days of exposure to air, no decomposition is found, and the PLQE maintains a high value (68.66%), demonstrating excellent air stability. Figure S3 shows the TGA-DTG data mentioned before; the first weight loss of 63.88 wt % observed at 328 and 395 °C is related to the decomposition of organic components $(C_9NH_{20})_2MnBr_4$. The decomposition reaction equation could proceed according to the following scheme: $(C_9NH_{20})_2MnBr_4 \rightarrow 2(C_9NH_{20}Br) + MnBr_2$. The second weight loss of 36.12 wt %, centered at around 646 °C, is attributed to the evaporation of $MnBr_2$. The above results show that this material can maintain good structural stability at

DOI: 10.1021/acs.inorgchem.9b02374
Inorg. Chem. 2019, 58, 13464−13470

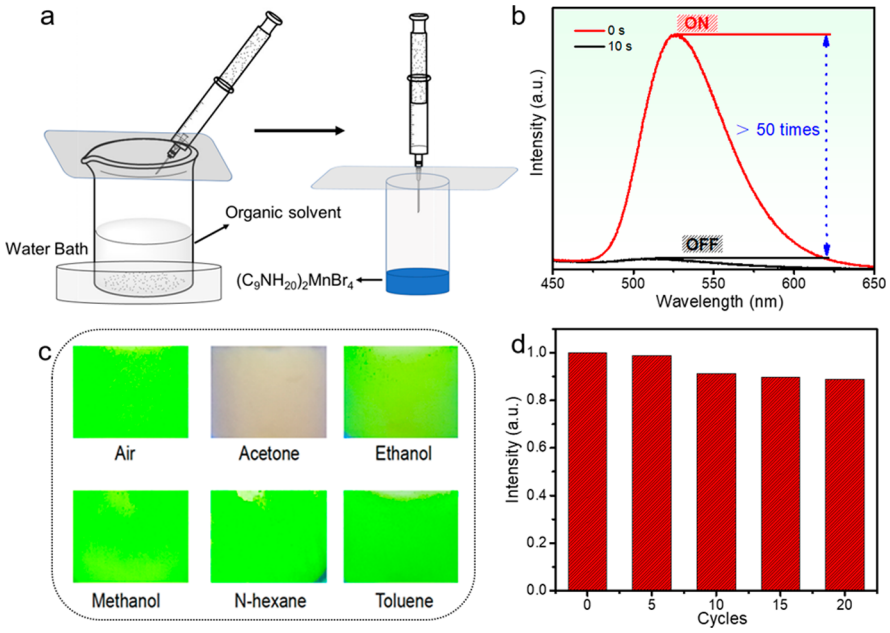

Figure 5. (a) Schematic diagram of a simplified device for gas sensing application. (b) Time-related emission spectra of $(C_9NH_{20})_2MnBr_4$ toward acetone vapor. (c) Digital photos of $(C_9NH_{20})_2MnBr_4$ upon exposure to various organic vapors for 10 min under 365 nm UV excitation. (d) PL intensity of $(C_9NH_{20})_2MnBr_4$ toward acetone vapor for 20 cycles.

about 240 °C. The photostability experiment under a high-power mercury lamp (300 mw cm^{-2}) with continuous irradiation illumination also verifies the high photostability (Figure S5).

DFT calculations are used to further understand the luminescent mechanism and the electronic structure of $(C_9NH_{20})_2MnBr_4$ by using the structural data obtained at 150 K. Figure 4a shows that $(C_9NH_{20})_2MnBr_4$ possesses a direct band gap of 4.485 eV with the valence band maximum (VBM) and the conduction band minimum (CBM) both at the G point, which is close to the experimental value (4.940 eV) (Figure S6). Figure 4b displays the calculated total and orbital-resolved partial densities of states (PDOS) for $(C_9NH_{20})_2MnBr_4$. The VBM is dominated by Mn 3d and Br 4p states, while the CBM is mainly contributed by Br 5s states. Because the organic part, C_9NH_{20}, has little contribution to the VB and CB, we consider that C_9NH_{20} has no contribution to the PL process. In addition, the flat bands of both VB and CB indicate that no obvious intermolecular coupling can be found between the $MnBr_4^{2-}$ species. Hence, we find that each individual $MnBr_4^{2-}$ can act as a separate luminescence center.

In general, the sudden quenching or shining of luminescence can be used as an effective way to detect toxic and volatile gases.[20,37,38] During the experiment, we noticed that the luminescence of $(C_9NH_{20})_2MnBr_4$ can be quickly quenched by acetone vapor. Thus, we explored the potential applications of $(C_9NH_{20})_2MnBr_4$ in the gas-sensing field. The simplified gas-sensitive detecting device is shown in Figure 5a. By detecting the PL spectra before exposure to acetone vapor and 10 s after exposure to acetone vapor (Figure 5b), we find that the strong green emission was weakened more than 50-fold within 10 s. Such good switchable behavior is the key to gas-sensing applications. Moreover, selectivity is another important indicator. Thus, the luminescence response of $(C_9NH_{20})_2MnBr_4$ upon exposure to different organic solvent vapors for 10 min was measured, and the corresponding digital photos of under 365 nm UV excitation are given in Figure 5c. No obvious fluorescence change was observed except for that to acetone vapor, which indicates that $(C_9NH_{20})_2MnBr_4$ has selective fluorescence quenching for acetone vapor in terms of several organic solvents currently selected. Finally, good reversibility and circulation is equally important. After 20 cycles, the PXRD patterns show no evidence of material decomposition (Figure S7), and the luminescence intensity does not drop significantly (Figure 5d), which shows that $(C_9NH_{20})_2MnBr_4$ has good reversibility and circulation. The above results indicate that $(C_9NH_{20})_2MnBr_4$ is a potential candidate for gas-sensing applications.

CONCLUSIONS

In summary, we designed and synthesized a novel 0D lead-free organic–inorganic metal halide $(C_9NH_{20})_2MnBr_4$. The detailed crystal structure and the temperature-dependent structural phase transition have been determined. A highly luminescent green emission peaking at 528 nm with a fwhm of 64 nm and a high PLQE of around 81.08% was observed at RT for this hybrid material, which is originated from the $^4T_1(G)$ to $^6A_1$ radiative transition of tetrahedrally coordinated Mn^{2+} ions in the $[MnBr_4]$ unit. $(C_9NH_{20})_2MnBr_4$ also demonstrates excellent moisture, heat, and light stability for the versatile application. Therefore, we have further developed a fluorescent sensor based on the as-prepared $(C_9NH_{20})_2MnBr_4$, suggesting a good switchable behavior, reversibility, circulation, and selectivity against different organic solvents, as an excellent system for fluorescent sensor applications. We believe that the current work will promote the design and preparation of new metal halide materials for luminescence sensor and probe applications.

ASSOCIATED CONTENT

Supporting Information

The Supporting Information is available free of charge on the ACS Publications website at DOI: 10.1021/acs.inorgchem.9b02374.

DOI: 10.1021/acs.inorgchem.9b02374
Inorg. Chem. 2019, 58, 13464−13470

Fractional atomic coordinates and isotropic or equivalent isotropic displacement parameters, main geometric parameters, EA analysis data, PXRD profiles, TGA-DTG data, CIE diagram, photoluminescence stability, and UV−vis diffuse reflectance spectra (PDF)

Accession Codes

CCDC 1945705 contains the supplementary crystallographic data for this paper. These data can be obtained free of charge via www.ccdc.cam.ac.uk/data_request/cif, or by emailing data_request@ccdc.cam.ac.uk, or by contacting The Cambridge Crystallographic Data Centre, 12 Union Road, Cambridge CB2 1EZ, UK; fax: +44 1223 336033.

AUTHOR INFORMATION

Corresponding Author

*E-mail: xiazg@scut.edu.cn.

ORCID

Xingxing Jiang: 0000-0001-6068-8773
Zheshuai Lin: 0000-0002-9829-9893
Jing Zhao: 0000-0002-8000-5973
Zhiguo Xia: 0000-0002-9670-3223

Author Contributions

#M.L. and J.Z. contributed equally to this work.

Notes

The authors declare no competing financial interest.

ACKNOWLEDGMENTS

This work is supported by the National Natural Science Foundation of China (Nos. 51722202 and 51972118), Natural Science Foundations of Beijing (2172036), the Fundamental Research Funds for the Central Universities (FRF-TP-18-002C1), and the Guangdong Provincial Science & Technology Project (No. 2018A050506004).

REFERENCES

(1) Saparov, B.; Mitzi, D. B. Organic-Inorganic Perovskites: Structural Ver satility for Functional Materials Design. *Chem. Rev.* **2016**, *116* (7), 4558−4596.

(2) Zhao, Y. X.; Zhu, K. Organic-inorganic hybrid lead halide perovskites for optoelectronic and electronic applications. *Chem. Soc. Rev.* **2016**, *45* (3), 655−689.

(3) Chen, K.; Li, L. Ordered Structures with Functional Units as a Paradigm of Material Design. *Adv. Mater.* **2019**, 1901115.

(4) Tian, W.; Zhou, H. P.; Li, L. Hybrid Organic-Inorganic Perovskite Photo detectors. *Small* **2017**, *13* (41), 1702107.

(5) Ahmadi, M.; Wu, T.; Hu, B. A Review on Organic-Inorganic Halide Perovskite Photodetectors: Device Engineering and Fundamental Physics. *Adv. Mater.* **2017**, *29* (41), 1605242.

(6) Hao, F.; Stoumpos, C. C.; Cao, D. H.; Chang, R. P. H.; Kanatzidis, M. G. Lead-free solid-state organic−inorganic halide perovskite solar cells. *Nat. Photonics* **2014**, *8* (6), 489−494.

(7) Tsai, H.; Nie, W.; Blancon, J. C.; Stoumpos, C. C.; Asadpour, R.; Harutyunyan, B.; Neukirch, A. J.; Verduzco, R.; Crochet, J. J.; Tretiak, S.; et al. High-efficiency two-dimensional Ruddlesden-Popper perovskite solar cells. *Nature* **2016**, *536* (7616), 312−316.

(8) Mao, L. L.; Ke, W. J.; Pedesseau, L.; Wu, Y. L.; Katan, C.; Even, J.; Wasielewski, M. R.; Stoumpos, C. C.; Kanatzidis, M. G. Hybrid Dion-Jacobson 2D Lead Iodide Perovskites. *J. Am. Chem. Soc.* **2018**, *140* (10), 3775−3783.

(9) Tan, Z. K.; Moghaddam, R. S.; Lai, M. L.; Docampo, P.; Higler, R.; Deschler, F.; Price, M.; Sadhanala, A.; Pazos, L. M.; Credgington, D.; Hanusch, F.; Bein, T.; Snaith, H. J.; Friend, R. H. Bright light-emitting diodes based on organometal halide perovskite. *Nat. Nanotechnol.* **2014**, *9* (9), 687−692.

(10) Kim, Y. H.; Cho, H.; Heo, J. H.; Kim, T. S.; Myoung, N.; Lee, C. L.; Im, S. H.; Lee, T. W. Multicolored organic/inorganic hybrid perovskite light-emitting diodes. *Adv. Mater.* **2015**, *27* (7), 1248−1254.

(11) Saidaminov, M. I.; Almutlaq, J.; Sarmah, S.; Dursun, I.; Zhumekenov, A. A.; Begum, R.; Pan, J.; Cho, N.; Mohammed, O. F.; Bakr, O. M. Pure Cs_4PbBr_6: Highly Luminescent Zero-Dimensional Perovskite Solids. *ACS Energy Letters* **2016**, *1* (4), 840−845.

(12) Roccanova, R.; Yangui, A.; Nhalil, H.; Shi, H.; Du, M.-H.; Saparov, B. Near-Unity Photoluminescence Quantum Yield in Blue-Emitting $Cs_3Cu_2Br_{5-x}I_x$ ($0 \le x \le 5$). *ACS Appl. Electron. Mater.* **2019**, *1* (3), 269−274.

(13) Jun, T.; Sim, K.; Iimura, S.; Sasase, M.; Kamioka, H.; Kim, J.; Hosono, H. Lead-Free Highly Efficient Blue-Emitting $Cs_3Cu_2I_5$ with 0D Electronic Structure. *Adv. Mater.* **2018**, *30* (43), 1804547.

(14) Zhou, C. K.; Lin, H. R.; Shi, H. L.; Tian, Y.; Pak, C.; Shatruk, M.; Zhou, Y.; Djurovich, P.; Du, M. H.; Ma, B. W. A Zero-Dimensional Organic Seesaw-Shaped Tin Bromide with Highly Efficient Strongly Stokes-Shifted Deep-Red Emission. *Angew. Chem., Int. Ed.* **2018**, *57* (4), 1021−1024.

(15) Zhou, C. K.; Lin, H. R.; Worku, M.; Neu, J.; Zhou, Y.; Tian, Y.; Lee, S.; Dju rovich, P.; Siegrist, T.; Ma, B. W. Blue Emitting Single Crystalline Assembly of Metal Halide Clusters. *J. Am. Chem. Soc.* **2018**, *140* (41), 13181−13184.

(16) Yangui, A.; Roccanova, R.; McWhorter, T. M.; Wu, Y.; Du, M.-H.; Saparov, B. J. C. o. M. Hybrid Organic−Inorganic Halides $(C_5H_7N_2)_2MBr_4$ (M = Hg, Zn) with High Color Rendering Index and High-Efficiency White-Light Emission. *Chem. Mater.* **2019**, *31* (8), 2983−2991.

(17) Zhang, R. L.; Mao, X.; Yang, Y.; Yang, S. Q.; Zhao, W. Y.; Wumaier, T.; Wei, D. H.; Deng, W. Q.; Han, K. L. *Angew. Chem., Int. Ed.* **2019**, *58* (9), 2725−2729.

(18) Zhou, J.; Li, M. Z.; Ning, L. X.; Zhang, R. L.; Molokeev, M. S.; Zhao, J.; Yang, S. Q.; Han, K. L.; Xia, Z. G. Broad-Band Emission in a Zero-Dimensional Hybrid Organic $[PbBr_6]$ Trimer with Intrinsic Vacancies. *J. Phys. Chem. Lett.* **2019**, *10* (6), 1337−1341.

(19) Nolan, E. M.; Lippard, S. J. A "turn-on" fluorescent sensor for the se lective detection of mercuric ion in aqueous media. *J. Am. Chem. Soc.* **2003**, *125* (47), 14270−14271.

(20) Che, S. Y.; Dao, R. N.; Zhang, W. D.; Lv, X. Y.; Li, H. R.; Wang, C. M. Designing an anion-functionalized fluorescent ionic liquid as an efficient and reversible turn-off sensor for detecting SO_2. *Chem. Commun.* **2017**, *53* (27), 3862−3865.

(21) Wang, X. D.; Wolfbeis, O. S.; Meier, R. J. Luminescent probes and sensors for temperature. *Chem. Soc. Rev.* **2013**, *42* (19), 7834−7869.

(22) Jiang, C. L.; Zhong, N.; Luo, C. H.; Lin, H. C.; Zhang, Y. Y.; Peng, H.; Duan, C. G. $(Diisopropylammonium)_2MnBr_4$: a multifunctional ferroelectric with efficient green-emission and excellent gas sensing properties. *Chem. Commun.* **2017**, *53* (44), 5954−5957.

(23) Han, D.; Shi, H. L.; Ming, W. M.; Zhou, C. K.; Ma, B. W.; Saparov, B.; Ma, Y. Z.; Chen, S. Y.; Du, M. H. Unraveling luminescence mechanisms in zero-dimensional halide perovskites. *J. Mater. Chem. C* **2018**, *6* (24), 6398−6405.

(24) Sheldrick, G. M. Crystal structure refinement with SHELXL. *Acta Crystallogr., Sect. C: Struct. Chem.* **2015**, *71*, 3−8.

(25) Spek, A L. *PLATON - A Multipurpose Crystallographic Tool*; Utrecht University: Utrecht, The Netherlands, 2008.

(26) Brandenburg, K.; Berndt, M. *DIAMOND-Visual Crystal Structure Information System*; Crustal Impact, 2004.

(27) *Topas: General profile and structure analysis software for powder diffraction data*, version 4; Bruker AXS: Karlsruhe, Germany, 2008.

(28) Clark, S. J.; Segall, M. D.; Pickard, C. J.; Hasnip, P. J.; Probert, M. I. J.; Refson, K.; Payne, M. C. First principles methods using CASTEP. *Z. Kristallogr. - Cryst. Mater.* **2005**, *220* (5-6), 567−570.

(29) Ceperley, D. M.; Alder, B. J. Ground state of the electron gas by a stochastic method. *Phys. Rev. Lett.* **1980**, *45* (7), 566.

DOI: 10.1021/acs.inorgchem.9b02374
Inorg. Chem. 2019, 58, 13464−13470

(30) Perdew, J. P.; Zunger, A. Self-interaction correction to density-functional approximations for many-electron systems. *Phys. Rev. B: Condens. Matter Mater. Phys.* **1981**, *23* (10), 5048.
(31) Xu, L.; Gao, J. X.; Chen, X. G.; Hua, X. N.; Liao, W. Q. A temperature-triggered triplex bistable switch in a hybrid multifunctional material: $[(CH_2)_4N(CH_2)_4]_2[MnBr_4]$. *Dalton. Trans.* **2018**, *47* (47), 16995−17003.
(32) Xu, L. J.; Sun, C. Z.; Xiao, H.; Wu, Y.; Chen, Z. N. Green-Light-Emit ting Diodes based on Tetrabromide Manganese(II) Complex through Solution Process. *Adv. Mater.* **2017**, *29* (10), 1605739.
(33) Lawson, K. E. Optical Studies of Electronic Transitions in Hexa and Tetracoordinated Mn^{2+} Crystals. *J. Chem. Phys.* **1967**, *47* (9), 3627−3633.
(34) Zhou, J.; Rong, X. M.; Zhang, P.; Molokeev, M. S.; Wei, P. J.; Liu, Q. L.; Zhang, X. W.; Xia, Z. G. Manipulation of Bi^{3+}/In^{3+} Transmutation and Mn^{2+}'Doping Effect on the Structure and Optical Properties of Double Perovskite $Cs_2NaBi_{1-x}In_xCl_6$. *Adv. Opt. Mater.* **2019**, *7* (8), 1801435.
(35) Zhou, G. J.; Guo, S. Q.; Zhao, J.; Molokeev, M.; Liu, Q. L.; Zhang, J. Y.; Xia, Z. G. Unraveling the mechanochemical synthesis and luminescence in MnII-based two-dimensional hybrid perovskite $(C_4H_9NH_3)_2PbCl_4$. *Sci. China. Mater.* **2019**, *62* (7), 1013−1022.
(36) Rodríguez-Lazcano, Y.; Nataf, L.; Rodríguez, F. Electronic structure and luminescence of$[(CH_3)_4N]_2MnX_4$(X = Cl,Br)crystals at high pressures by time-resolved spectroscopy: Pressure effects on the Mn-Mn exchange coupling. *Phys. Rev. B: Condens. Matter Mater. Phys.* **2009**, *80* (8), 085115.
(37) Li, P.; Zhang, Y. Z.; Wang, Y. G.; Wang, Y. J.; Li, H. R. Luminescent euro pium(III)-beta-diketonate complexes hosted in nanozeolite L as turn-on sensors for detecting basic molecules. *Chem. Commun.* **2014**, *50* (89), 13680−13682.
(38) Xue, P. C.; Sun, J. B.; Yao, B. Q.; Gong, P.; Zhang, Z. Q.; Qian, C.; Zhang, Y.; Lu, R. Strong emissive nanofibers of organogels for the detection of volatile acid vapors. *Chem. - Eur. J.* **2015**, *21* (12), 4712−4720.

DOI: 10.1021/acs.inorgchem.9b02374
Inorg. Chem. 2019, 58, 13464−13470